ASSESSMENT OF DEGRADATION OF RAILROAD RAILS:
FINITE ELEMENT ANALYSIS OF INSULATED JOINTS AND
UNSUPPORTED SLEEPERS

Hossam Elsayed, Mohamed Lotfy, Haytham Zohny and Hany Sobhy

msp

ASSESSMENT OF DEGRADATION OF RAILROAD RAILS: FINITE ELEMENT ANALYSIS OF INSULATED JOINTS AND UNSUPPORTED SLEEPERS

HOSSAM ELSAYED, MOHAMED LOTFY, HAYTHAM ZOHNY AND HANY SOBHY

This research investigates the response of rail material using an elastic-plastic finite-element framework. The implications of unsupported sleepers and insulated rail joints which represent sources of stiffness discontinuity in railroad lines were included. The nonlinear response of wheel-rail material was considered. The developed finite-element model has been supported by an analytical method to assess the onset of fatigue cracks in rails. Deflections, strains, stresses, and crack initiation parameters were obtained. The results showed good compatibility with the field observations, Hertz's theory, and equivalent studies. The findings showed the high sensitivity of plastic flow and rail material fatigue to the value of rail deflection which on the contrary has a meagre impact on the magnitudes of stresses. In addition, insulated rail joints due to stress singularity have a hurtful influence on the quantities of stresses, plastic deformation, and fatigue life. However, this effect plummets with increasing depth. For all cases, cracks initiate at the rail's surface knowing that the simulated friction coefficient between wheel and rail is 0.35 and the applied wheel load is 110 kN. Additionally, 15 mm depth is enough to study the nonlinear characteristics of rail materials. And finally, unsupported sleepers accelerate the electrical failure, which causes troublesome traffic disturbances, at insulated rail joints.

1. Introduction

Deterioration of rails is a critical and growing issue for railways across the world. Zerbsta et al. [2009] stated that in Great Britain over the last century the failures of rails per train kilometre have been raised more than twice. In Egypt, for reasons still not rigorously identified, rail fracture is inevitable and frequent every year (see Figure 1) with a plethora of replacements taking place prior to the complete damage (not included in Figure 1). This problem is not only contributing to increasing the annual costs of maintenance [Cannon et al. 2003] but also it may cause catastrophic incidents such as the derailment of Hatfield train in the UK which resulted in four fatalities and over seventy casualties [Zerbsta et al. 2009]. This issue reaches its maxima at the locations where the track losses its stiffness continuity. Such discontinuity can be found at the insulated rail joints (IRJs) (or in short insulated joints) which are used to control the railway signalling system of most modern rail networks. At any IRJ, it is required to have two rails electrically insulated from each other with an insulating material which always has lower stiffness than the adjacent rails inducing high-stress concentration at IRJ's zone. Zong and Dhanasekar [2014] highlighted that the average life of IRJs is 20% compared with conventional rails, making their replacement about 20%–50% of the entire track replacements. Another source of stiffness irregularity appears at unsupported sleepers (or hanging sleepers), which refer to sleepers connected to the rail
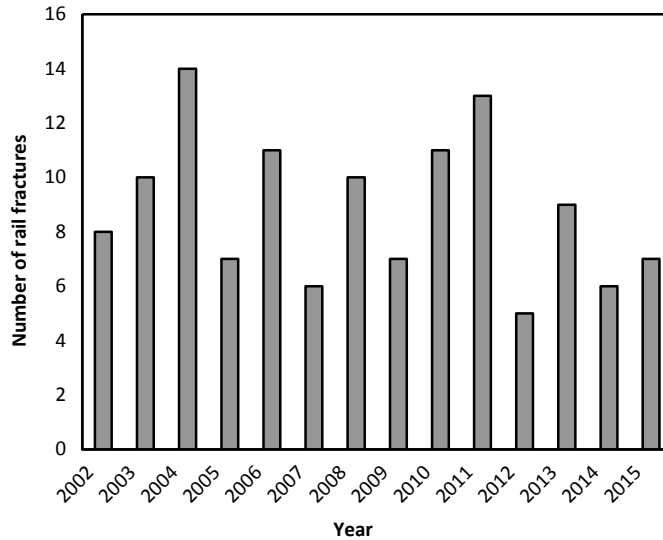
Figure 1. Variation of the number of rail fractures per year in the first line of Cairo Metro in Egypt [El-sayed et al. 2018a].

without any support from the ballast. This fault is created by the uneven settlement of the ballast or the underneath material layer formed during service life due to irregularity in track stiffness [Lundqvist and Dahlberg 2005]. This defect exists in all ballasted railroad lines. Augustin et al. [2003] claimed that in reality up to 50% of sleepers are partially or fully hanging. Olsson and Zackrisson [2002] found by field measurements very frequent small gaps among sleepers and ballast, with different size of these gaps of the same sleeper. Ishida et al. [1999] explained with an analytical dynamic model the baleful effect of unsupported sleepers on the fatigue life of rail welds, rail deflection, and rail bending stress.

The likelihood of the occurrence of hanging sleepers at IRJs is high. This can be explained in Figure 2. The reduction of stiffness at IRJ's location intensifies the dynamic forces [Wen et al. 2005; Cai et al. 2007; Pang and Dhanasekar 2006], causing track deterioration through a various number of failure modes [Mandal and Peach 2010; Rathod et al. 2012; El-sayed et al. 2018b]; e.g., squashing, spalling, rolling contact fatigue, plastic flow in the proximity of the joint, and sleepers' failure. These failure forms make a ferocious cycle with the quantity of impact load. As the train-track dynamic load escalated, the nonuniform deformation of the ballast increases [Zhang et al. 2008; Grassie and Cox 1985], producing unsupported sleepers' defect. In the literature, most of the efforts investigate either the effects of unsupported sleepers [Ishida et al. 1999; Zhang et al. 2008; Grassie and Cox 1985; Bezin et al. 2009] or IRJs [Chen and Chen 2006; Chen and Kuang 2002; Zong and Dhanasekar 2012; Sandström and Ekberg 2009] on the behaviour of railway track. However, both issues jointly should be studied for real knowledge of the mechanisms of rail's failure. Likewise, although the fatigue life and stress-strain states have been extensively explored for conventional rails [El-sayed et al. 2018a; Ringsberg 2001; Ringsberg et al. 2000; Ringsberg and Josefson 2001] and rails at traditionally bolted joints [Wen et al. 2005; Cai et al. 2007; Mohammadzadeh et al. 2013], the impact of IRJs and hanging sleepers simultaneously and separately on these dilemmas is questionable.
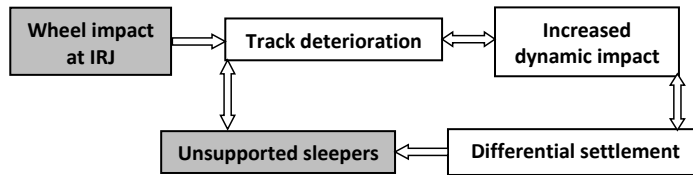
Figure 2. The process of unsupported sleepers' formation at IRJ.

This research focuses on examining the influence of IRJs in collaboration with hanging sleepers on the rail material response and comparing the results with that acquired from each issue individually. To this end, numerical simulations were implemented in which different scenarios for comparison purpose were created accounting for both normal and jointed tracks in the absence and presence of hanging sleepers considering the whole track response. The plastic deformation, realistic contact geometry, and rail bending were considered, which are necessary to get authentic findings. The numerical results were discussed and compared against field investigation, Hertz's theory, and equivalent studies. Likewise, they were incorporated with a fatigue life criterion to get predictions of the initiation of fatigue cracks in rails.

2. Modelling of wheel-track system

To achieve the research objective, a three-dimensional (3D) finite element (FE) model was performed considering the full wheel-track system with the implementation of an elastic-plastic material model using ABAQUS/Explicit code [Dassault Systèmes 2014]. The introduced model is based on specifications of a sector of railroad track existing in Cairo Metro (CM), Egypt; it is hereafter named the test site and it is depicted minutely in [Egyptian National Railways 2004]. At the test site, the standard 1435 mm gauge is used. A 54E1 (UIC54) standard rail profile (Figure 3, second row, left) with an inclination of 1 : 20 is applied and supported by monoblock concrete sleepers (Figure 3, third row). The sleeper spacing is 0.6 m and each sleeper is embedded into a ballast layer, which has a depth of 0.3 m. The sleeper is separated from the rail bottom with a layer of compressible material (rail pad) of 5 mm height and a steel plate of 14 mm thickness. The wheel has a nominal radius R_w of 510 mm (Figure 3, second row, right), subjected to a vertical static load equal to 110 kN when there are 13 passengers per meter square in the motorcoach. The peak permissible (design) speed of the trains passing the test site is 100 km/h while the operational speed is 80 km/h.

2.1. *Modelling of normal track.* The normal track model here refers to the track with no irregularity. Referring to Figure 3, two FE models were created namely "global model" and "submodel". The global model is used to account for the bending line of rail. The influence of rail pads, sleepers, ballast, and subgrade was considered (see Figure 3, top row, left). The rail pad was connected with the rail and sleeper in both vertical and transverse directions. The steel base plate existing under the rail pad was disregarded since its impact on the rail bending is quite small because of its higher stiffness compared with other components beneath the rail. The ballast and subgrade layers were connected by tie constraints with no longitudinal displacement permitted at the ends of the two layers. The base of the model and the ends of the rail were fixed in all directions. Symmetry of the track system was presumed so that only one wheel and a half-straight track were modelled with symmetry boundary condition assigned at the
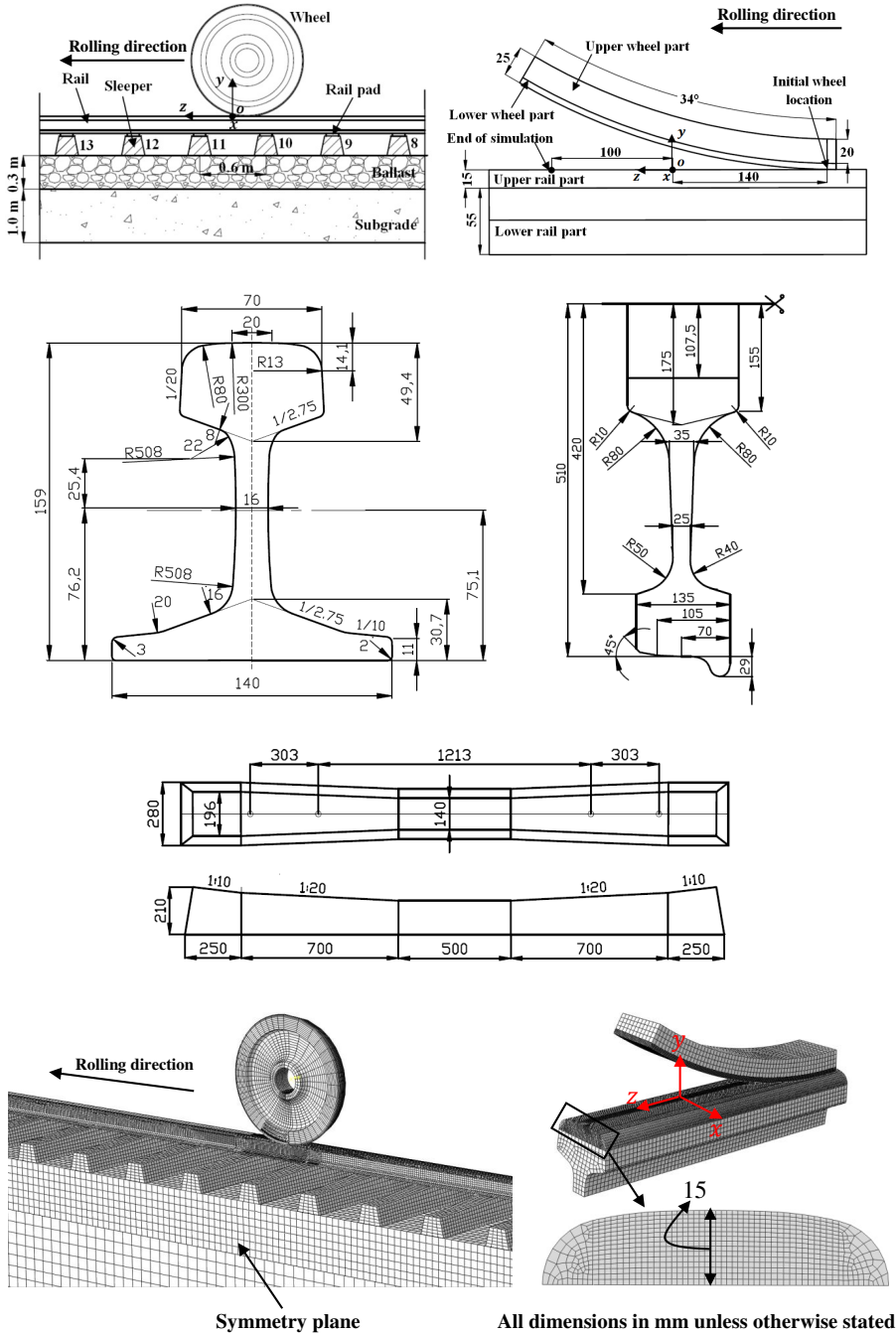
Figure 3. Wheel-track interaction model. Top row: schematic diagram of a part of the global FE model (left) and representation of the wheel-rail FE model in submodel (right). Second row: rail profile (left) and wheel profile (right). Third row: dimensions of a concrete monoblock sleeper (the plane is drawn above the longitudinal view). Bottom row: meshing of a section of the global model (left) and meshing of submodel (right).

symmetry plane. This system was modelled for a length of 20 sleeper spans which is long enough to simulate the track response [Sadeghi 1997]. Such large FE model prohibits element size to be refined to a desirable level due to barriers of calculation time which passively affects the fineness of local stresses and strains generated at the region of wheel-rail interface. Accordingly, using submodeling approach, which enables examining a local sector of the entire model with a much finer mesh and with no disregard of the rail bending line [Dassault Systèmes 2014], another FE model dubbed as "submodel" was created. This model as clarified in Figure 3 (top row, right) is composed of only a limited sector of the wheel and rail. The response of rail's boundaries with time in submodel was acquired from the global model. For the same reason of calculation time, the rolling distance in both models was restrained to 240 mm. The initial contact position among wheel-rail was taken at 140 mm away from the origin o of coordinate system $oxyz$ defined in Figure 3 (top row) where the origin o is located at the middle-top point of the 54E1 (UIC54) profile, at the mid-side of the two middle sleepers, i.e., sleeper 10 and sleeper 11. The current and previous studies [El-sayed et al. 2018a; 2018b] have shown that this length using the explicit analysis method in case of elastic-plastic behaviour can give reliable results. The meshed geometry is demonstrated in Figure 3 (bottom row, left and right) for the global model and submodel, respectively. The modelled wheel and rail parts were meshed with first-order brick elements (Type C3D8) with fine elements, 2 mm × 2 mm × 2 mm and 1 mm × 1 mm × 0.8 mm in the global model and submodel, in x, y, z, respectively, at the contact area; while, coarse mesh was allowed at other noncontacting regions. The mesh transition among regions of different element characteristics was managed using tie constraints. For other components reduced integrated solid elements (Type C3D8R) were preferred since they minify the time of calculation and exhibit no shear locking. The material parameters of the FE model are given in Table 1, in which the variables defining the nonlinear response of wheel-rail materials are also presented. These parameters obtained from [El-sayed et al. 2018a] are compatible with the test site's specifications. The elastic-plastic behaviour was implemented only in submodel at the contact spot; i.e., the upper rail part and the lower wheel part (Figure 3, top row, right). Other than that, the elastic response was applied.

2.2. *Modelling of unsupported sleepers.* As presented in Figure 4, two hanging sleepers were considered to be unsupported; namely sleeper 10 and sleeper 11, the two middle sleepers. These hanging sleepers were modelled by introducing a gap with 2 mm and 4 mm between the two sleepers and the ballast bed. Shi et al. [2012], according to measurement carried out by Guangzhou Railway Corporation in China [Li and Sun 1992] clarified that the range of small gaps among sleepers and ballast is 2 mm to 4 mm. In the simulation, the interaction between the hanging sleepers and ballast was activated only when the prescribed gap was closed. The transition from the normal track sector to the unsupported one was not studied; only the unsupported area was elucidated to explore the effect of increased deflection on material failure.

2.3. *Modelling of jointed railway track.* As clarified in Figure 5 (left), the modelled IRJ as utilized at the test site is composed of an insulating material inserted between two rail sections. This layer is made of fibreglass material and its width is 8 mm. To secure the joint, two steel joint bars are fastened to the rails with epoxy adhesive and six pretensioned bolts. The adhesive layers were presumed to have a thickness of 3 mm. The joint bar has nonuniform cross-sections as seen in Figure 5 (right), shaped with thicker mid-section (width = 48 mm) to provide additional strength and deflection resistance at the joint's region. In the simulation, the end post and adhesive layers were assumed to be fully bonded with

Part	Parameter (Unit)	Value
Wheel (grade R7)	Mass density, ρ_w (kg/m^3)	7850
	Elastic modulus, E_w (MPa)	205000
	Poisson's ratio, ν_w	0.3
	Yield stress, σ_{yw} (MPa)	316
	Kinematic hardening parameter, γ	401
	Kinematic hardening modulus, C (MPa)	137000
Rail (grade 900A)	Mass density, ρ_r (kg/m^3)	7800
	Elastic modulus, E_r (MPa)	206000
	Poisson's ratio, ν_r	0.28
	Yield stress, σ_{yr} (MPa)	379
	Kinematic hardening parameters, $\gamma_1, \gamma_2, \gamma_3$	55, 600, 2000
	Kinematic hardening modules, C_1, C_2, C_3 (MPa)	24750, 60000, 200000
	Isotropic hardening parameter, R	500
	Isotropic hardening modulus, Q_∞ (MPa)	-189
Rail pad	Mass density, ρ_p (kg/m^3)	950
	Elastic modulus, E_ρ (MPa)	800
	Poisson's ratio, ν_p	0.46
Sleeper	Mass density, ρ_c (kg/m^3)	2300
	Elastic modulus, E_c (MPa)	36000
	Poisson's ratio, ν_c	0.3
Ballast	Mass density, ρ_b (kg/m^3)	1800
	Elastic modulus, E_b (MPa)	170
	Poisson's ratio, ν_b	0.3
Subgrade	Mass density, ρ_s (kg/m^3)	1600
	Elastic modulus, E_s (MPa)	30
	Poisson's ratio, ν_s	0.25

Table 1. Material parameters applied in the numerical simulations [El-sayed et al. 2018a].
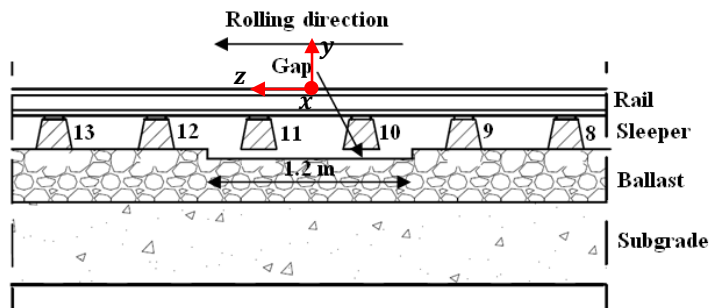

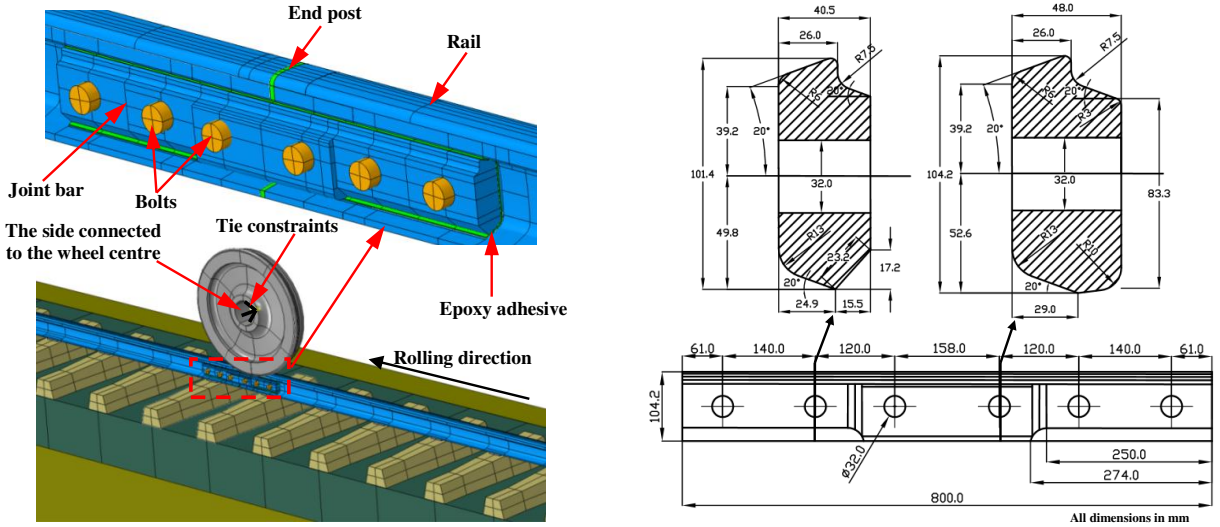**Figure 4.** Schematic drawing of hanging sleepers.

Figure 5. Left: global overview of a part of the wheel-track model with IRJ. Right: mechanical drawing of the joint bar.

the adjacent steel material. The nuts and washers were not accounted for since they do not contribute to the joint's stiffness. The IRJ in this research is located over the two middle sleepers and the origin o of IRJ's scenarios is at the centre of 54E1 (UIC54) profile and at the surface of rail edge 1, the first edge in the rolling direction. In submodel analysis, the presence of end post layer is the only difference compared to the normal track model (Section 2.1). The joint bars, bolts, epoxy adhesive, and end post were considered to behave elastically and modelled using C3D8R elements. The joint bars and bolts were deemed to have the same elastic properties of rail steel (Table 1); whilst, the epoxy adhesive and end post were presumed to have a modulus of elasticity of 4500 MPa, Poisson's ratio of 0.19, and density of 1920 kg/m^3. These properties were used in other previous studies [Chen and Kuang 2002].

2.4. *Applied loads.* Loads and rolling of the wheel were negotiated by three quantities F_y, V, and ω defined at the central point of the wheel. This point was rigidly linked by tie constraints with all nodes of the closest side of the wheel part (see Figure 5, left). Here, F_y is the vertical force taken equivalent to 110 kN. Displacement of the wheel was achieved by imposing a translational velocity V at the wheel centre. To simulate pure rolling, an angular velocity ω equal to V/R_w was applied. Since the trains at the site concerned move with a design speed of 100 km/h, a translational velocity of 100 km/h with an angular one equal 54.5 rad/s were applied to the wheel. The wheel was not allowed to move in the lateral direction and no lateral forces were applied to the model. For insulated joint's scenarios, in the global model, the bolt pretension load generated from bolt tightening was considered. The bolt pretension P_b can be defined as [Wen et al. 2005]

$$P_b = \frac{T}{K_b D},\tag{1}$$

where K_b is the coefficient of the bolt torque moment T, and D is the bolt diameter. Here, the selected values are $T = 500$ Nm [Wen et al. 2005], $K_b = 0.2$ [Wen et al. 2005], and $D = 32$ mm according to IRJ's design used in CM.

2.5. *Wheel-track interaction.* In the FE-software, the interface was defined by surface-to-surface discretization algorithm. One surface of this approach is called "master surface" and the other is "slave surface". Contact was then achieved by forbidding nodes of the slave surface in each increment from penetrating the master segment using a penalty algorithm which imposes normal springs among the penetrating nodes and the master surface. The contact force is equal to the product of contact stiffness and penetration distance. Isotropic Coulomb's friction model was adopted to simulate the tangential behaviour with a limiting shear stress value of μP at the contacting nodes where slip takes place. Here, μ is the friction coefficient, and P is the interface pressure. If the frictional stress is lower than μP, a penalty algorithm was used to ensure that no slip occurs. The value of μ was selected as 0.35 for wheel-rail interface [Harrison et al. 2002], 0.3 for rail-rail pad and rail pad-sleeper interfaces [Zhang 2015], 0.7 for sleeper-ballast layer interface [Zhang 2015], and 0.4 for bolts-joint bars and bolts-rails interfaces [Cai et al. 2007]. The finite sliding option was permitted during analysis to define the relative sliding among the two contacting bodies. The wheel-rail contact position was presumed at the lateral centre of the rail profile against the wheel tread.

3. Results and discussion

The results are discussed for the performed scenarios, which are:

Scenario 1: Normal track.

Scenario 2: Track with two hanging sleepers of 2 mm gap size.

Scenario 3: Track with an IRJ.

Scenario 4: Incorporation of scenario 2 with scenario 3.

Scenario 5: Track with two unsupported sleepers of 4 mm gap size.

Scenario 6: Integration of scenario 3 with scenario 5.

The last two scenarios are presented only when there is an obvious impact of increasing gap size from 2 mm to 4 mm.

3.1. *Displacement.* As depicted in Figure 6 (left), the crest downward displacement of scenario 1 is 1.95 mm which is concurrent with El-sayed et al. [2018a] with 8% difference owing to the finer meshing implemented in this study. Another reason is that in [El-sayed et al. 2018a] the length of the modelled track is equivalent to 32 sleeper spans being different from the FE model created here in which 20 sleepers were utilized. In scenario 2, the climax downward deflection is 3.87 mm, extensively higher compared with that acquired from scenario 1 due to low stiffness. This abrupt change of rail displacement at the region of hanging sleepers would cause undesirable effects on ride comfort and safety. However, the impact of IRJ on the magnitude of this component is relatively small (not exceed 2.7%). This means that such joint bar design (see Figure 5, right) provides adequate stiffness to the rail joint in the vertical direction. The impact of gap size on the peak values of rail deflection is clarified in Figure 6 (right). It is obvious that the relationship between gap size and rail downward deflection is nonlinear. As the gap size increased from 2 mm to 4 mm, the maximum downward deflection raised only by 16.6% in the absence of IRJ and by 13.7% in the presence of IRJ. This behaviour is probably due to the impact of the adjacent sleepers. Adding these findings to that obtained in [Ishida et al. 1999], it can be concluded that there
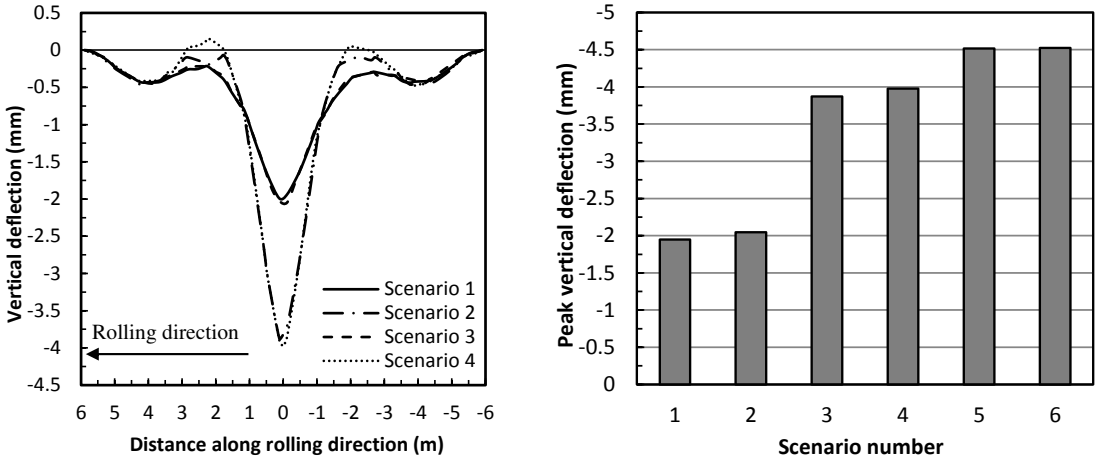
Figure 6. Left: deflection of rail for the first four scenarios. Right: effect of gap size on the maximum downward deflection of the rail.

is a gap size above which the rail deflection is unchanging, and the unsupported sleepers don't touch the ballast. Figure 7 depicts the residual longitudinal deformation at the end of the loading step at IRJ's region for scenario 3 and scenario 4 as obtained from submodel analysis. As clarified, the width of end post dwindled due to the axial deformation of rail material adjacent to IRJ's zone. The peak reduction of IRJ's width for both scenarios occurred at $y = -0.8$ mm with a magnitude equal to 0.1874 mm and 0.2486 mm for scenario 3 and scenario 4, respectively, meaning that hanging sleepers can markedly accelerate the electrical deterioration of IRJs, which occurs if the two rails at IRJ's zone touched each other when the track of this section is not occupied. This electrical problem causes troublesome traffic disturbances.
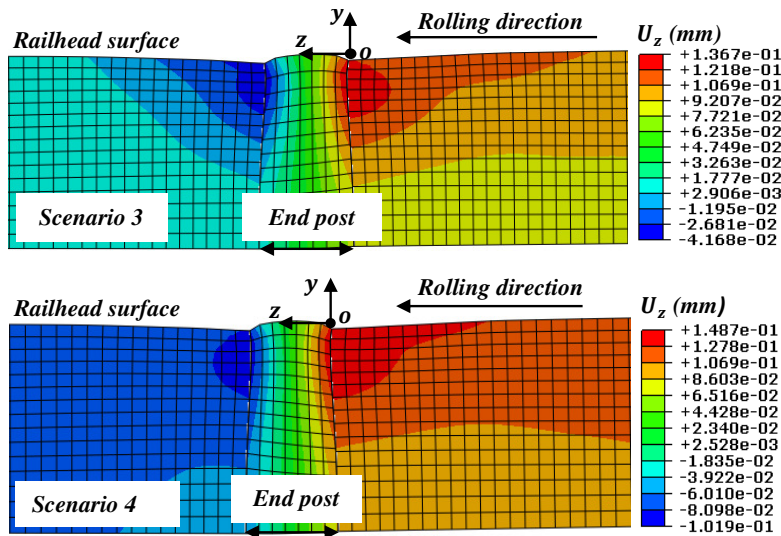
Figure 7. Residual longitudinal deformation at IRJ's region (deformation scale factor = 10).

3.2. *Surface pressure.* The interface pressure distribution at the position which has peak value during rolling contact is plotted in Figure 8. However, it should be recognized that as the rail is discretely supported, the contact characteristics alter with the change of contact position, see Figure 12 (left) for more clarification. As depicted in scenario 1, the normal pressure is maxima when $P = 1000$ MPa distributed over a contact area of 21.49 mm and 18.01 mm in z-direction and x-direction, respectively. Compared with Hertz's theory which is based on elastic behaviour assumption, refer to [Johnson 1985] for detailed illustration, the present FE model as depicted in Figure 9, owing to the consideration of plastic deformation, showed a lower pressure value with a larger contact patch in both directions. These findings are in good agreement with that obtained in [Yan and Fischer 2000]. On the contrary with scenario 1, the peak magnitude of pressure is largely unaffected by the existence of hanging sleepers, the difference is only 1.67%, but the position of this value is different, it appeared closer to the track origin. This position remained the same as the gap size increased from 2 mm to 4 mm. For scenario 3, as expected a high impact on interface pressure parameters (shape and magnitude) due to edge effect was obtained. The entity of IRJ raised the peak value of interface pressure to 1172 MPa, which is 17.2% larger than that computed from scenario 1. Moreover, the contact spot became wider in z-direction and in x-direction as well. In scenario 4, case of hanging sleepers with IRJ, the pressure value increased by 4.35% from that determined in scenario 3 with no change in the location of crest pressure value.
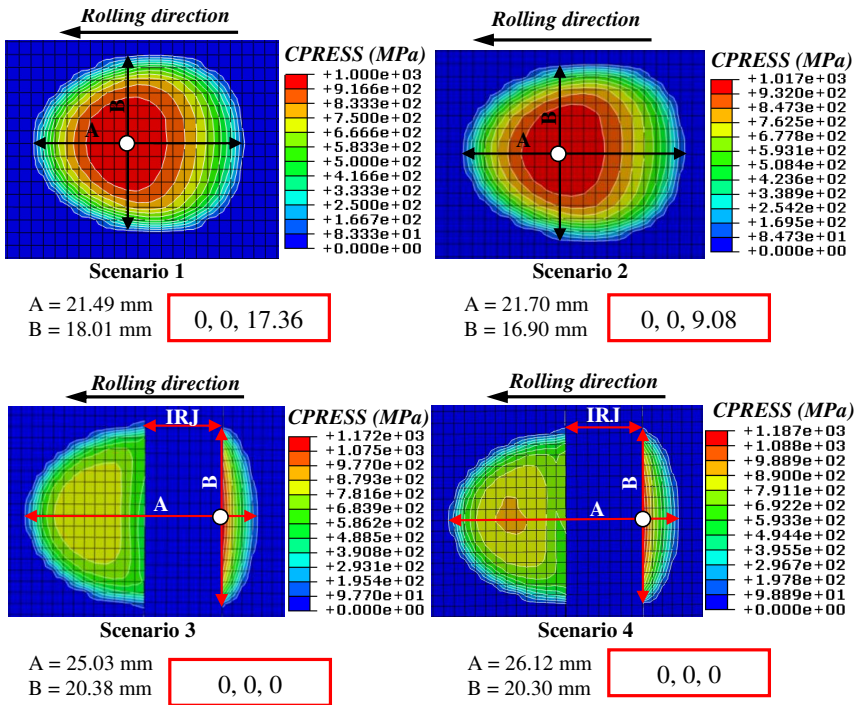

Figure 8. Interface pressure's distribution for the first four scenarios when the contact pressure reached its climax value. Note, A and B represent dimensions of the contact patch in rolling and lateral directions, respectively, and the white point shows the position of peak pressure value whose coordinates are drawn in a red box.
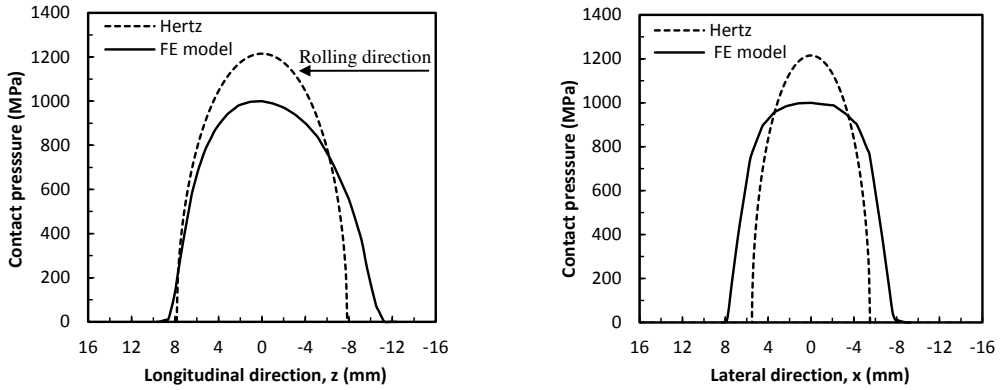
Figure 9. Distribution of contact pressure acquired from the FE model in scenario 1 and Hertz's theory: along the rolling axis (left) and along the lateral axis (right). Here, the origin is placed at the crest P value.

The tangential stress distribution at the crest normal pressure position is delineated in Figure 10. In scenario 1 and scenario 2, the magnitude of surface shear stress is lower than μP along the contact spot. This means that the contact patch is totally in stick due to the free-rolling condition. The reason for the small negative tangential stress quantity, existing in the leading edge of the contact patch, is that the tangential force is negligible at this location, case of frictionless contact. However, in scenario 3 and scenario 4, despite free-rolling, the tangential stress distribution coincides with the corresponding μP curve up to rail edge 1 where interfacial shear stress hit its maximum magnitude. Furthermore, because of the significant reduction of interface pressure at the end post as presented in Figure 8, the direction of surface shear stress is opposite on both sides of the IRJ correlating well with the results gained in [Chen and Chen 2006]. The effect of hanging sleepers on increasing the tangential stress of IRJ's scenarios is only obvious on the left side of the IRJ. These results reveal the meagre effect of rail deflection on wheel-rail contact characteristics.
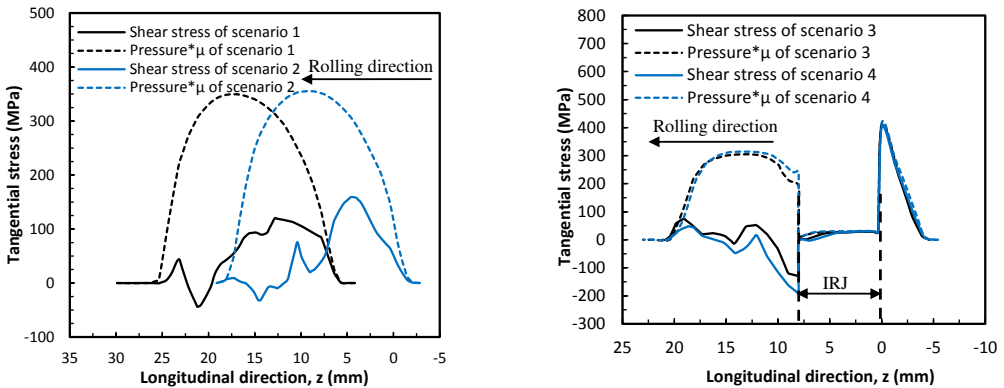

Figure 10. Surface shear stress distribution along the z-axis: for scenarios without IRJ (left) and for IRJ's scenarios (right). Solid lines represent the tangential shear stress (τ_{yz}) and dashed lines represent the interface pressure multiplied by μ (i.e., $P\mu$).

3.3. *Stress analysis.* Figure 11 depicts the contours of von Mises stress σ_e in x-y plane from the FE model together with the distribution of σ_e along the rail depth at $x = 0$ for the four main scenarios. These plots were drawn when σ_e reached its maximum value. As clarified, the crest value of σ_e (denoted by black point) formed at the rail's surface with a value equal 514.8 MPa and 506.5 MPa in scenario 1 and scenario 2, respectively, noticeably larger than the yield strength of rail material which is 379 MPa in this analysis. In addition, in both scenarios the magnitudes of σ_e remain almost constant to some millimetres beneath the rail surface. This could increase the probability of both surface and subsurface damage initiation. For IRJ's scenarios, the peak σ_e magnitude located at the rail's top surface at $z = 0$, then it decreased rapidly. Compared with scenario 1, the vicinity of IRJ again due to edge effect increased the summit σ_e magnitude by 46.36% and 43.42% in scenario 3 and scenario 4, respectively. However, at subsurface depths, approximately 4 mm below the surface, the behaviour reversed. Moreover, the effect of hanging sleepers on this component is quite small along the upper rail part, being analogous with the results presented in Section 3.2. This means that von Mises stress magnitude is highly influenced by the contact characteristics and rail displacement has a minuscule impact on this quantity.

Figure 12 (left) indicates the crest von Mises stress σ_e magnitude in a strip of surface nodes along the travelling direction at $x = 0$. The peak stress of a node is the maximum stress the node experienced in the time history. As observed, for all given scenarios the characteristics of von Mises stress, such as values and shapes (not shown in the figure), differ with time even with smooth rail surface. This is because of both the vibrations of the track system which are inherent in the explicit model and the change of contact spot position on a discretely supported system. The results showed that, the oscillation amplitude of σ_e in scenario 1 is 47.01 MPa, 10.53% of the mean value which equal 446.55 MPa. For scenario 2, the oscillation amplitude is 69.11 MPa, 15.80% of the mean value that is equivalent to 437.41 MPa. This implies that on the contrary to the normal track, the stress oscillation increases in case of unsupported sleepers. In the IRJ's scenarios, the entity of insulating layer changed drastically the oscillation amplitude which equals 253.52 MPa and 239.1 MPa in scenario 3 and scenario 4, respectively, in the studied strip.

3.4. *Plastic strain analysis.* As seen in Figure 12 (right), the maximum value of equivalent plastic strain ε_{eff} in the first two scenarios appeared at subsurface and at different longitudinal position, precisely at $y = -2.54$ mm and $z = 35.20$ mm for scenario 1 and at $y = -4.19$ mm and $z = 74.36$ mm for scenario 2. These results contradict with the von Mises stress contours depicted in Figure 11 in which the peak stress is on the surface. This behaviour occurs because of the rail deflection. El-sayed et al. [2018a] compared a FE model that considered rail bending with another one that neglected this factor and the results explained that a 1.805 mm vertical deflection makes the maximum ε_{eff} quantity appearing at subsurface; while the zenith von Mises stress value is on the top. In addition, the peak ε_{eff} value is 0.009625 and 0.013018 in scenario 1 and scenario 2, respectively; i.e., the hanging sleepers alone incremented the crest ε_{eff} value by 35.25%. The increase of gap size from 2 mm to 4 mm reduced the crest ε_{eff} value for unsupported sleepers' scenarios without IRJ by 21.67% and made the maximum value appearing at $y = -4.25$ mm and $z = 22.75$ mm. These findings emphasise that the ε_{eff} quantity is sensitive to the value of vertical rail displacement. By combining these outcomes with that computed in [El-sayed et al. 2018a], one can conclude that the plastic deformation in continuous rails increases as the rail deflection rises to a certain value, then the plastic flow reduces again. However, this quantity is largely uninfluenced by the presence of hanging sleepers alongside IRJ. For scenario 3 and scenario 4, the climax value of ε_{eff} emerged at
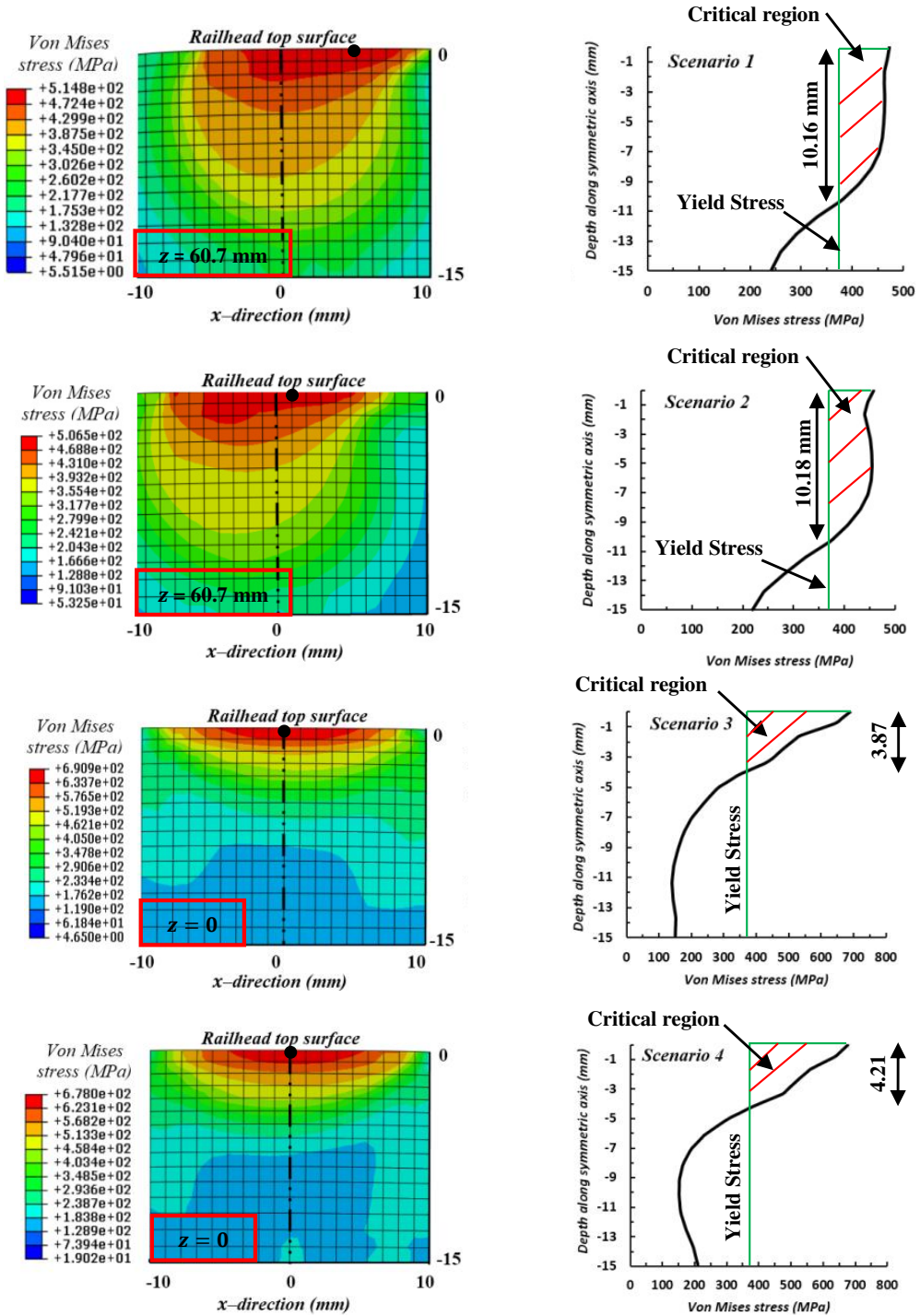
Figure 11. Contours of von Mises stress in x-y plane associated with the variation of σ_e along the rail depth at $x = 0$ for the first four studied scenarios. The red box denotes the position of section in the longitudinal direction.
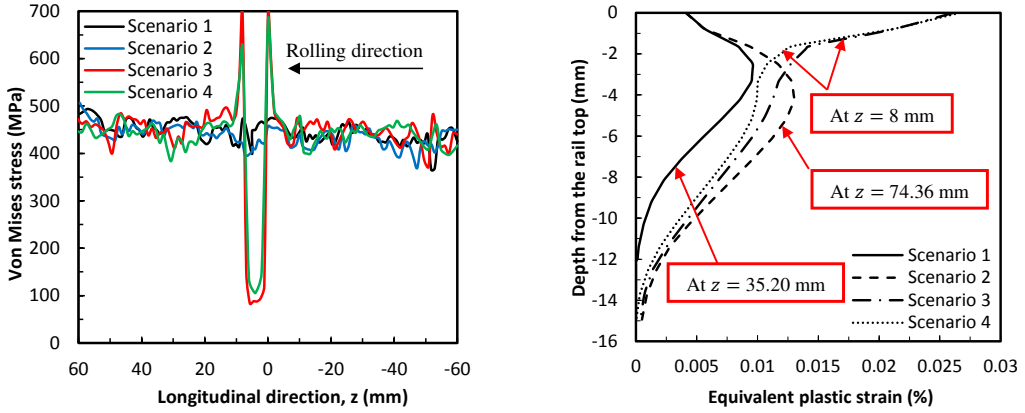
Figure 12. Left: peak von Mises stress of a strip of surface nodes in the travelling direction at $x = 0$. Right: variation of equivalent plastic strain ε_{eff} with rail depth for the first four scenarios at the location where the peak magnitude of ε_{eff} is observed.

the top of rail edge 2, which is slightly larger than that obtained at rail edge 1, see Figure 13 for more illustration, with a magnitude equal 0.026117 and 0.026633. These values are corresponding to 2.71 and 2.77 times of that computed from scenario 1. Then, the quantity of ε_{eff} decreased swiftly like the trend of von Mises stress seen in Figure 11. With regard to the dimensions of plastic region, the depth of plastic zone is 11.97 mm in scenario 1; whilst for those scenarios which include either hanging sleeper defect or IRJ, the depth of plastic zone exceeded with a quite small value the 15 mm depth which signifies that the presumed dimensions of plastic layer implemented in this research are widely adequate to recognize the nonlinear response of rail material.
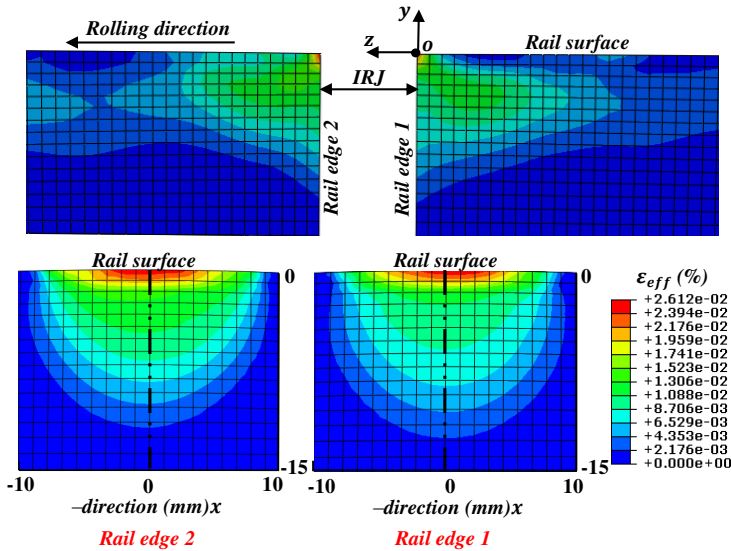
Figure 13. Contours of equivalent plastic strain ε_{eff} at the perfect insulated joint scenario (scenario 3).

4. Fatigue crack initiation analysis

4.1. *Fatigue Model.* The high stresses induced by wheel-rail interface could increase the likelihood of damage initiation. Subsequently, with time, this leads to rail fracture and vehicle derailment. Therefore, it is necessary to quantify the fatigue impact. The results extracted from the FE model (Figure 14, for instance), revealed the multiaxial and nonproportional state of both stress and strain of the elements at the contact region. Hence, in the present study, the critical plane concept together with the multiaxial fatigue criterion proposed in [Jiang and Sehitoglu 1999] was employed to identify the effect of hanging sleepers and IRJs on the reliability of rail steel against crack initiation due to fatigue. Such combination has been shown to fit very well with experimental findings regarding both fatigue life and crack plane orientation [Chen et al. 1999; Varvani-Farahani 2000]. This method can be expressed with the multiaxial fatigue parameter

$$\text{FP} = \langle\sigma_{\max}\rangle\frac{\Delta\varepsilon}{2} + J\Delta\tau\Delta\gamma. \tag{2}$$

At a material plane under consideration, $\Delta\varepsilon$ is the range of the normal strain, and $\sigma_{\max}$ is the largest normal stress with $\langle\sigma_{\max}\rangle = \sigma_{\max}/2$ for $\sigma_{\max} > 0$ and $\langle\sigma_{\max}\rangle = 0$ for $\sigma_{\max} \leq 0$. Furthermore, $\Delta\tau$ is the range of shear stress, $\Delta\gamma$ is the range of shear strain, and J is a material parameter.

The fatigue parameter FP is related to the fatigue initiation life Nf via the relation

$$\text{FP}_{\max} = \frac{(\tau_f')^2}{G_r}(2Nf)^{2b} + \tau_f'\,\gamma_f'(2Nf)^{b+c}, \tag{3}$$

where $\text{FP}_{\max}$ is the peak fatigue parameter corresponding to the critical plane; τ_f', γ_f', b, and c are material parameters; $G_r = E_r/2(1 + \nu_r)$ is the shear modulus of rail. The mechanical properties used in fatigue calculations are $b = -0.089$, $c = -0.559$, $\gamma_f' = 15.45$, $\tau_f' = 468$ MPa, and $J = 0.2$ [Ringsberg 2001]. Nevertheless, the grade of rail steel employed at the test site is 900A, the prescribed values of fatigue parameters are corresponding to BS11 normal grade steel owing to lack of experimental data of grade 900A and the wide analogy of the mechanical properties of both two grades [Ringsberg et al. 2000; Ringsberg and Josefson 2001].
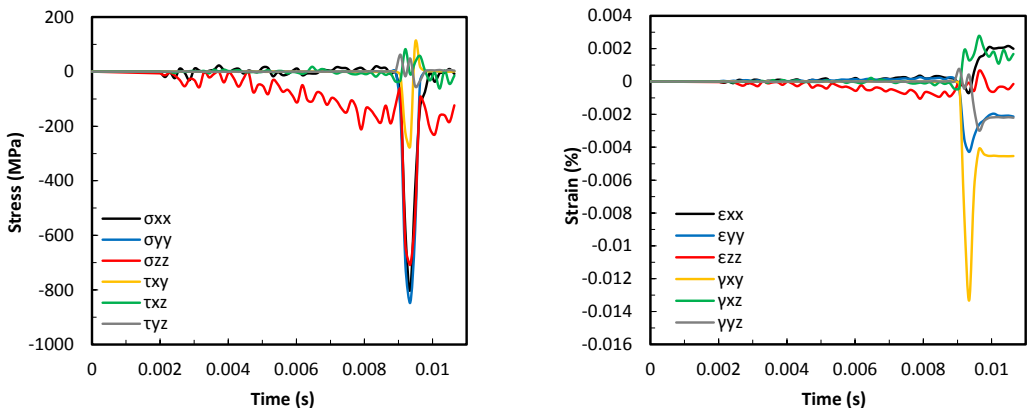

Figure 14. Variation of stress and strain components with time for the element experiencing peak von Mises stress in scenario 2.

4.2. *Numerical predictions of fatigue impact.* In the current research, the crack plane and the highest damage parameter were identified by the rotation of stress and strain tensors at an equal increment (1 degree) for a set of points suffering from maximum von Mises stress, at which damage is quite probable. Shear stress range $\Delta\tau$ and shear strain range $\Delta\gamma$ in (2) were identified by means of the longest chord method [Papadopoulos 1998]. The first part of (2) was removed due to the compression state of the three normal stress components (Figure 14). The crack plane was identified by two angles depicted in Figure 15. Angle θ is the angle between the normal vector $\vec{n}$ and z-axis; whilst angle φ is the angle between z-axis and crack plane. The variations of FP with the angles θ and φ for scenario 1 and scenario 2 as two samples are presented in Figure 16. These plots refer to the most critical point in each scenario where FP_{max} is obtained.

As shown in Table 2, the critical plane in scenario 1 occurred at $\theta = 111°$, $\varphi = 87°$, and $d = 0$. Field results presented in Figure 17 (left) indicate that the predominant orientation of cracks on the surface, corresponding to angle θ, lies between 113° and 123° which is in a good correlation with that predicted. Note that, the cracks at the test site were deemed to be initiated after being visible on the rail surface, but theoretically the crack may be treated to be initiated when its length is between 0.1 mm–0.5 mm
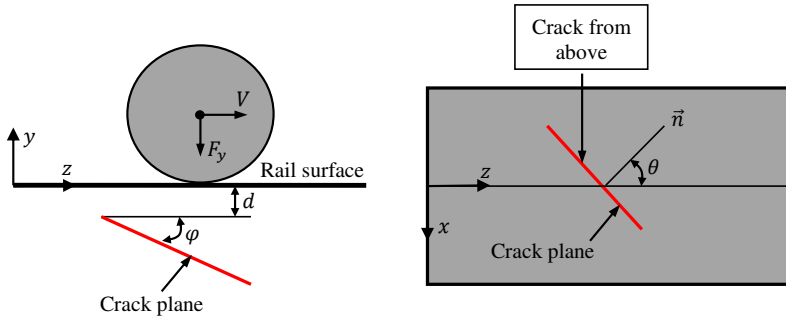
Figure 15. Definition of crack plane angles in the railhead.
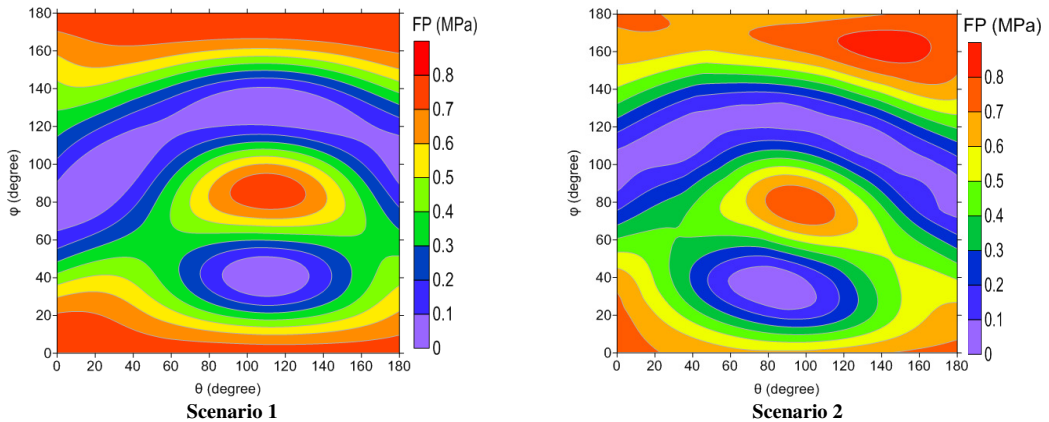
Figure 16. Variation of fatigue parameter with plane orientation in the first two scenarios for the critical point that showed the highest fatigue parameter value.

Scenario number	Description Hanging sleepers (gap size)	IRJ	θ (degree)	φ (degree)	Coordinates x	y	z	FP_{max} (MPa)	$N_r \cdot 10^5$ (passage)
1	No	No	111	87	0	0	60.72	0.7812	10.54
2	Yes (2 mm)	No	144	162	2.97	0	57.34	0.8403	9.176
3	No	Yes	174	111	0	0	0	2.3319	1.498
4	Yes (2 mm)	Yes	156	24	0	0	0	2.4152	1.412
5	Yes (4 mm)	No	84	84	1.86	0	58.46	0.8683	8.628
6	Yes (4 mm)	Yes	153	27	0	0	0	2.3059	1.527

Table 2. Predicted results of crack angles, crack coordinates, maximum fatigue parameter, and crack initiation life in each studied case.

[Ringsberg 2001]. However, angle φ contradicts with that estimated in [El-sayed et al. 2018a] where $\varphi = 9°-27°$. This is likely because of cyclic loading on material hardening considered in [El-sayed et al. 2018a] and disregarded in the present research. Likewise, the FP_{max} computed at the critical plan is 0.7812 MPa. This maximum quantity causes the crack to initiate after $1.054 \cdot 10^6$ wheel passages. Upon data collected from the test site about traffic volume, approximately 18576 axles pass the test site per day. This means that the crack in the studied loading condition initiates after 56 days, but this is a critical value because in this research the highest possible wheel load was chosen, and the action of wear which can mitigate rail material fatigue [Wang et al. 2009] was overlooked. This implies that the cracks in the test site probably initiate after the predicted period. In scenario 2 compared with scenario 1, a high deviation of the critical plane angles with a slight difference in position was observed. In addition, the FP_{max} in this scenario is higher than that evaluated from scenario 1 by 7.56%, which is corresponding to 12.94% reduction in the fatigue life. As the gap size increased from 2 mm to 4 mm, the fatigue life reduced again by 6.35%.

In scenario 3, the predicted location of cracks and the angle θ at the IRJ correlate well with the observations, see Figure 17 (right) as an example. Generally, it is obvious that in IRJ's scenarios the life
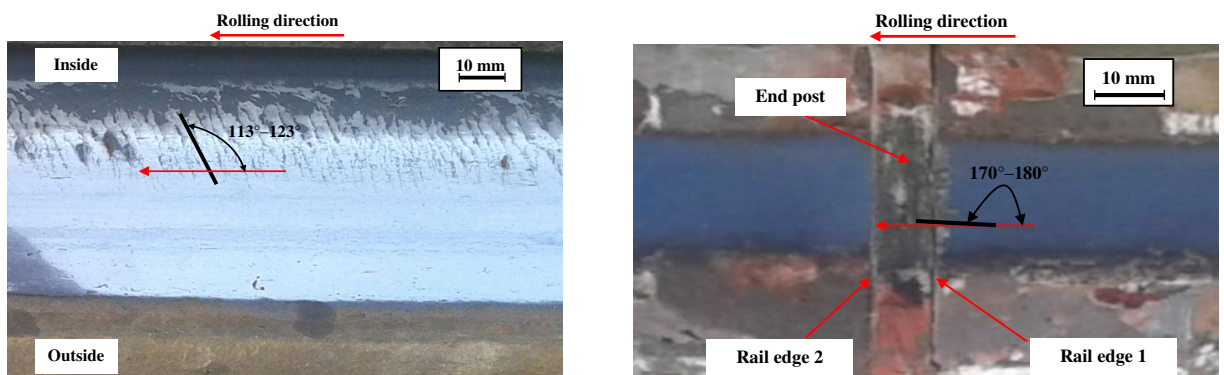

Figure 17. Observed defects on the railhead surface at the test site at the initiation stage: at a normal rail (left) and at an IRJ after three days of installation in the field (right). The given angle range is the predominate values along the test site.

of fatigue largely declines and the position of FP_{max} occurs at the surface of rail edge 1. The main cause of this is ratchetting, excessive plastic flow.

5. Conclusions

The behaviour of rail material in both normal and jointed railway tracks with and without hanging sleepers was analysed considering different scenarios. A three-dimensional finite-element model was built to compute displacements, stresses, and strains. The finite-element results were incorporated with a multiaxial fatigue model to comprehend the mechanism of crack initiation in rails. The main findings are summed up as follows:

- In comparison with the normal track model, the track with hanging sleepers exhibits higher magnitudes of deflection, stress oscillation (as quantified by von Mises stress), and plastic strain. In addition, unsupported sleepers reduce the fatigue life of the rail material.

- The quantity and position of plastic flow are highly sensitive to the value of rail deflection. On the contrary, the interface parameters (interface pressure, tangential stress, and contact area) and von Mises stress values are largely unaffected by this factor.

- At insulated joints, stiffness discontinuity at end post has a detrimental impact on the rail material, particularly at rail's edges. From the studied case compared with the normal track model, the model with insulated joint mounted the peak magnitudes of interface pressure, von Mises stress, and plastic strain by 17.2%, 46.36%, and 177%, respectively. In addition, due to the ratchetting response of the material at rail's edges, the fatigue life is severely reduced.

- The seriousness of insulated joints is increased if integrated with hanging sleepers. The increments due to this incorporation for the case of 2 mm gap size in comparison with the perfect insulated track model in rail deflection, joint width reduction, and fatigue life are 94.43%, 32.66%, and 6.09%, respectively. However, a marginal increase in the fatigue life was found in the model of insulated joint with 4 mm gap size. The higher reduction of the joint width in the entity of hanging sleepers accelerates the deterioration of insulated joints from the electrical viewpoint.

- Based on the obtained results, it is recommended that the track maintenance operators should consider a strategy to avoid the appearance or development of hanging sleepers.

References

[Augustin et al. 2003] S. Augustin, G. Gudehus, G. Huber, and A. Schünemann, "Numerical model and laboratory tests on settlement of ballast track", pp. 317–336 in *System dynamics and long-term behaviour of railway vehicles, track and subgrade*, vol. 6, edited by K. Popp and W. Schiehlen, Lecture Notes in Applied Mechanics, Springer, Berlin, Heidelberg, 2003.

[Bezin et al. 2009] Y. Bezin, S. D. Iwnicki, M. Cavalletti, E. de Vries, F. Shahzad, and G. Evans, "An investigation of sleeper voids using a flexible track model integrated with railway multi-body dynamics", *Proc. Inst. Mech. Eng. F* **223**:6 (2009), 597–607.

[Cai et al. 2007] W. Cai, Z. Wen, X. Jin, and W. Zhai, "Dynamic stress analysis of rail joint with height difference defect using finite element method", *Eng. Fail. Anal.* **14**:8 (2007), 1488–1499.

[Cannon et al. 2003] D. F. Cannon, K.-O. Edel, S. L. Grassie, and K. Sawley, "Rail defects: an overview", *Fatigue Fract. Eng. Mater. Struct.* **26** (2003), 865–887.

[Chen and Chen 2006] Y.-C. Chen and L.-W. Chen, "Effects of insulated rail joint on the wheel/rail contact stresses under the condition of partial slip", *Wear* **260**:11-12 (2006), 1267–1273.

[Chen and Kuang 2002] Y. C. Chen and J. H. Kuang, "Contact stress variations near the insulated rail joints", *Proc. Inst. Mech. Eng. F* **216**:4 (2002), 265–273.

[Chen et al. 1999] X. Chen, S. Xu, and D. Huang, "A critical plane-strain energy density criterion for multiaxial low-cycle fatigue life under non-proportional loading", *Fatigue Fract. Eng. Mater. Struct.* **22** (1999), 679–686.

[Dassault Systèmes 2014] Dassault Systèmes, *ABAQUS analysis user's guide*, 6.14, Dassault Systèmes Simulia Corp, 2014, Available at http://130.149.89.49:2080/v6.14/pdf_books/ANALYSIS_4.pdf.

[Egyptian National Railways 2004] Egyptian National Railways, *Guidelines for railways and switches maintenance*, Railway Engineering Department, 2004.

[El-sayed et al. 2018a] H. M. El-sayed, M. Lotfy, H. N. El-din Zohny, and H. S. Riad, "Prediction of fatigue crack initiation life in railheads using finite element analysis", *Ain Shams Eng. J.* **9**:4 (2018), 2329–2342.

[El-sayed et al. 2018b] H. M. El-sayed, M. Lotfy, H. N. El-din Zohny, and H. S. Riad, "A three dimensional finite element analysis of insulated rail joints deterioration", *Eng. Fail. Anal.* **91** (2018), 201–215.

[Grassie and Cox 1985] S. L. Grassie and S. J. Cox, "The dynamic response of railway track with unsupported sleepers", *Proc. Inst. Mech. Eng. D* **199**:2 (1985), 123–136.

[Harrison et al. 2002] H. Harrison, T. McCanney, and J. Cotter, "Recent developments in coefficient of friction measurements at the rail/wheel interface", *Wear* **253**:1-2 (2002), 114–123.

[Ishida et al. 1999] M. Ishida, T. Moto, A. Kono, and Y. Jin, "Influence of loose sleeper on track dynamics and bending fatigue of rail welds", *Q. Rep. RTRI* **40**:2 (1999), 80–85.

[Jiang and Sehitoglu 1999] Y. Jiang and H. Sehitoglu, "A model for rolling contact failure", *Wear* **224**:1 (1999), 38–49.

[Johnson 1985] K. L. Johnson, *Contact mechanics*, Cambridge University Press, Cambridge, 1985.

[Li and Sun 1992] Z. F. Li and J. G. Sun, "Maintenance and cause of unsupported sleeper", *China Railway Building* **2** (1992), 15–17.

[Lundqvist and Dahlberg 2005] A. Lundqvist and T. Dahlberg, "Load impact on railway track due to unsupported sleepers", *Proc. Inst. Mech. Eng. F* **219**:2 (2005), 67–77.

[Mandal and Peach 2010] N. K. Mandal and B. Peach, "An engineering analysis of insulated rail joints: a general perspective", *Int. J. Eng. Sci. Technol.* **2**:8 (2010), 3964–3988.

[Mohammadzadeh et al. 2013] S. Mohammadzadeh, M. Sharavi, and H. Keshavarzian, "Reliability analysis of fatigue crack initiation of railhead in bolted rail joint", *Eng. Fail. Anal.* **29** (2013), 132–148.

[Olsson and Zackrisson 2002] E. L. Olsson and P. Zackrisson, "Long-term measurement results", technical report 2B/000120/T2/DA for the EUROBALT II Project, Final report, Banverket, Borlänge, 2002.

[Pang and Dhanasekar 2006] T. Pang and M. Dhanasekar, "Dynamic finite element analysis of the wheel-rail interaction adjacent to the insulated rail joints", in *Proc. of the 7th International Conference of Contact Mechanics and Wear of Wheel/Rail Systems (CM 2006)* (Brisbane), 2006.

[Papadopoulos 1998] I. V. Papadopoulos, "Critical plane approaches in high-cyclic fatigue on the definition of the amplitude and mean value of the shear stress acting on the critical plane", *Fatigue Fract. Eng. Mater. Struct.* **21** (1998), 269–285.

[Rathod et al. 2012] C. Rathod, D. Wexler, T. Chandra, and H. Li, "Microstructural characterisation of railhead damage in insulated rail joints", *Mater. Sci. Forum* **706-709** (2012), 2937–2942.

[Ringsberg 2001] J. W. Ringsberg, "Life prediction of rolling contact fatigue crack initiation", *Int. J. Fatigue* **23**:7 (2001), 575–586.

[Ringsberg and Josefson 2001] J. W. Ringsberg and B. L. Josefson, "Finite element analyses of rolling contact fatigue crack initiation in railheads", *Proc. Inst. Mech. Eng. F* **215**:4 (2001), 243–259.

[Ringsberg et al. 2000] J. W. Ringsberg, H. Bjarnehed, A. Johansson, and B. L. Josefson, "Rolling contact fatigue of rails — finite element modelling of residual stresses, strains and crack initiation", *Proc. Inst. Mech. Eng. F* **214**:1 (2000), 7–19.

[Sadeghi 1997] J. Sadeghi, *Investigation of characteristics and modeling of railway track system*, Ph.D. thesis, Department of Civil and Mining Engineering, University of Wollongong, 1997, Available at https://ro.uow.edu.au/theses/1249/.

[Sandström and Ekberg 2009] J. Sandström and A. Ekberg, "Numerical study of the mechanical deterioration of insulated rail joints", *Proc. Inst. Mech. Eng. F* **223**:3 (2009), 265–273.

[Shi et al. 2012] J. Shi, A. H. Chan, and M. P. N. Burrow, "Influence of unsupported sleepers on dynamic responses of railroad embankment below a heavy haul railway line using simulation techniques", in *Proc. of Rail Research UK Association Annual Conference*, 2012.

[Varvani-Farahani 2000] A. Varvani-Farahani, "A new energy-critical plane parameter for fatigue life assessment of various metallic materials subjected to in-phase and out-of-phase multiaxial fatigue loading conditions", *Int. J. Fatigue* **22**:4 (2000), 295–305.

[Wang et al. 2009] W. J. Wang, J. Guo, Q. Y. Liu, M. H. Zhu, and Z. R. Zhou, "Study on relationship between oblique fatigue crack and rail wear in curve track and prevention", *Wear* **267**:1-4 (2009), 540–544.

[Wen et al. 2005] Z. Wen, X. Jin, and W. Zhang, "Contact-impact stress analysis of rail joint region using the dynamic finite element method", *Wear* **258**:7-8 (2005), 1301–1309.

[Yan and Fischer 2000] W. Yan and F. D. Fischer, "Applicability of the Hertz contact theory to rail-wheel contact problems", *Arch. Appl. Mech.* **70**:4 (2000), 255–268.

[Zerbsta et al. 2009] U. Zerbsta, R. Lundénb, K.-O. Edel, and R. A. Smith, "Introduction to the damage tolerance behaviour of railway rails – a review", *Eng. Fract. Mech.* **76**:17 (2009), 2563–2601.

[Zhang 2015] Z. Zhang, *Finite element analysis of railway track under vehicle dynamic impact and longitudinal loads*, Master's thesis, Civil & Environmental Engineering, University of Illinois at Urbana-Champaign, 2015, Available at https://www.ideals.illinois.edu/handle/2142/89060.

[Zhang et al. 2008] S. Zhang, X. Xiao, Z. Wen, and X. Jin, "Effect of unsupported sleepers on wheel/rail normal load", *Soil Dyn. Earthq. Eng.* **28**:8 (2008), 662–673.

[Zong and Dhanasekar 2012] N. Zong and M. Dhanasekar, "Analysis of rail ends under rail contact loading", *Int. J. Mechan. Mechatron. Eng.* **6**:8 (2012), 1469–1477.

[Zong and Dhanasekar 2014] N. Zong and M. Dhanasekar, "Experimental studies on the performance of rail joints with modified wheel/railhead contact", *Proc. Inst. Mech. Eng. F* **228**:8 (2014), 857–877.

HOSSAM ELSAYED: houssam.mohamed91@eng.suez.edu.eg
Civil Engineering Departement, Faculty of Engineering, Suez Canal University, Ismailia 41522, Egypt

MOHAMED LOTFY: lotfytaha@cu.edu.eg
Aerospace Department, Faculty of Engineering, Cairo University, Giza 12316, Egypt

HAYTHAM ZOHNY: hnzohny@eng.asu.edu.eg
Public Works Departement, Faculty of Engineering, Ain Shams University, Cairo 11517, Egypt

HANY SOBHY: hanysobhyr@eng.asu.edu.eg
Public Works Departement, Faculty of Engineering, Ain Shams University, Cairo 11517, Egypt

JOURNAL OF MECHANICS OF MATERIALS AND STRUCTURES

msp.org/jomms

Founded by Charles R. Steele and Marie-Louise Steele

Journal of Mechanics of Materials and Structures